Proangiogenic scaffolds as functional templates for cardiac tissue engineering

Lauran R. Madden[a,1], Derek J. Mortisen[b,1], Eric M. Sussman[a], Sarah K. Dupras[c], James A. Fugate[c], Janet L. Cuy[a], Kip D. Hauch[a], Michael A. Laflamme[a,c], Charles E. Murry[a,c], and Buddy D. Ratner[a,b,2]

[a]Department of Bioengineering and [b]Department of Chemical Engineering, University of Washington, Seattle, WA 98195; and [c]Center for Cardiovascular Biology, Department of Pathology, University of Washington, Seattle, WA 98109

Edited by Robert Langer, Massachusetts Institute of Technology, Cambridge, MA, and approved July 15, 2010 (received for review May 25, 2010)

We demonstrate here a cardiac tissue-engineering strategy addressing multicellular organization, integration into host myocardium, and directional cues to reconstruct the functional architecture of heart muscle. Microtemplating is used to shape poly(2-hydroxyethyl methacrylate-co-methacrylic acid) hydrogel into a tissue-engineering scaffold with architectures driving heart tissue integration. The construct contains parallel channels to organize cardiomyocyte bundles, supported by micrometer-sized, spherical, interconnected pores that enhance angiogenesis while reducing scarring. Surface-modified scaffolds were seeded with human ES cell-derived cardiomyocytes and cultured in vitro. Cardiomyocytes survived and proliferated for 2 wk in scaffolds, reaching adult heart densities. Cardiac implantation of acellular scaffolds with pore diameters of 30–40 μm showed angiogenesis and reduced fibrotic response, coinciding with a shift in macrophage phenotype toward the M2 state. This work establishes a foundation for spatially controlled cardiac tissue engineering by providing discrete compartments for cardiomyocytes and stroma in a scaffold that enhances vascularization and integration while controlling the inflammatory response.

angiogenesis | cardiomyocyte | human embryonic stem cell | hydrogel

To date, most cell-based strategies for cardiac repair inject cell suspensions directly into injured myocardium. Studies show that 50–90% of injected cells are lost by extrusion (1) and that ∼90% of remaining cells die within 1 wk of implantation (2). Another class of cell-based therapies creates organized tissue constructs in vitro that can be conditioned before myocardial implantation. A scaffold system scaled to address diffusion limitations of static culture may enhance cell delivery by facilitating cell retention and survival. The ideal scaffold would provide compartmentalization, organizing cardiomyocytes within the scaffold into anisotropic fibers before implantation. This ideal scaffold also would provide void spaces for vasculature and stroma. Hence, the engineered construct would create macroscopic tissue that is structurally analogous to native tissue and would facilitate host integration.

The ability of cardiomyocytes to self-aggregate and survive in suspension culture led several groups to engineer tissue constructs of cells only (3–5) or of cells and extracellular matrix proteins (6–8). Scaffolds may promote oriented tissue architectures that facilitate diffusion-based mass transfer to reduce the ischemic injury often encountered in cell aggregates or cell transplantation (9). A scaffold can also promote survival and integration by enhancing neovascularization while minimizing fibrotic encapsulation (10). Preliminary results suggested that a synthetic scaffold of spherical, interconnected, and tightly controlled pore sizes (30–40 μm in diameter) can vascularize rapidly in vivo with reduced fibrotic response (10, 11). This porous scaffold can be fabricated to impose structural organization, such as cardiomyocytes into aligned fibers for electrical propagation and synchronous contraction (12). Mechanical matching of the scaffold to host myocardium can permit load transfer to grafted cardiomyocytes to stimulate maturation and contractile coupling while minimizing tissue damage. In this study, a bimodal scaffold architecture provides parallel channels to develop cardiomyocyte muscle bundles in vitro and also to develop a surrounding sphere-templated, interconnected porous network for improved mass transfer to generate larger tissue constructs. Implantation studies show that acellular, sphere-templated, porous constructs are able to direct rapid angiogenesis and minimize fibrosis in heart muscle.

Results

Polymer Fiber Templating. We fabricated poly(2-hydroxyethyl methacrylate-co-methacrylic acid) (pHEMA-co-MAA) hydrogel scaffolds with parallel channels by polymer fiber templating (13) (Fig. 1 *A* and *B*). Porous channel walls were interconnected to a spherical pore network using microsphere templating (10). Fabricated constructs resembled the structure and hierarchical organization of native myocardium. Channel size and spacing were controlled by varying the dimensions of the template fiber (45- to 150-μm diameter). We chose the smallest diameter compatible with reliable cell seeding, 60 μm, to alleviate mass transfer issues within the channel. Channel spacing of 60 μm was selected to allow introduction of pores ranging from 20–40 μm. In this configuration (Fig. 1 *A* and *B*), channels account for 25% of scaffold volume; the remaining 75% is a porous network of ∼60% void space.

Polymer Mechanics. Hydrogel mechanical properties can be tuned by cross-linking. Here, the elastic modulus of the solid polymer (155 ± 14 kPa) is similar to that of rat myocardium (590 ± 22 kPa) (14), whereas porous constructs (12 ± 6 kPa) are one order of magnitude lower than myocardial tissue and two orders of magnitude below myocardial scar tissue (4,700 ± 1,400 kPa) (14). We reasoned that tuning the scaffold modulus below that of myocardium would facilitate mechanical stimulation of engrafted cells in vivo while minimizing diastolic dysfunction associated with stiff infarct scar tissue.

High-Density Scaffold Seeding. Scaffolds initially were seeded with primary chicken embryonic-derived cardiomyocytes (∼20–25% cardiomyocytes). This model showed we could seed constructs at high cell densities (Fig. 1 *C* and *D*). Immunostaining against sarcomeric myosin, a striated muscle marker, showed that cardiomyocytes predominantly occupied the channels (Fig. 1*E*), whereas nonmyocytes migrated into the porous network and scaffold edge. Nonmyocyte proliferation choked off oxygen and nutrients to cardiomyocytes, limiting their viability to within ∼150 μm of the construct surface.

Author contributions: L.R.M., D.J.M., K.D.H., M.A.L., C.E.M., and B.D.R. designed research; L.R.M., D.J.M., E.M.S., S.K.D., J.A.F., and J.L.C. performed research; L.R.M., D.J.M., E.M.S., K.D.H., M.A.L., C.E.M., and B.D.R. analyzed data; and L.R.M., D.J.M., E.M.S., K.D.H., M.A.L., C.E.M., and B.D.R. wrote the paper.

The authors declare no conflict of interest.

This article is a PNAS Direct Submission.

[1]L.R.M. and D.J.M. contributed equally to this work.

[2]To whom correspondence should be addressed. E-mail: ratner@uweb.engr.washington.edu.

This article contains supporting information online at www.pnas.org/lookup/suppl/doi:10.1073/pnas.1006442107/-/DCSupplemental.

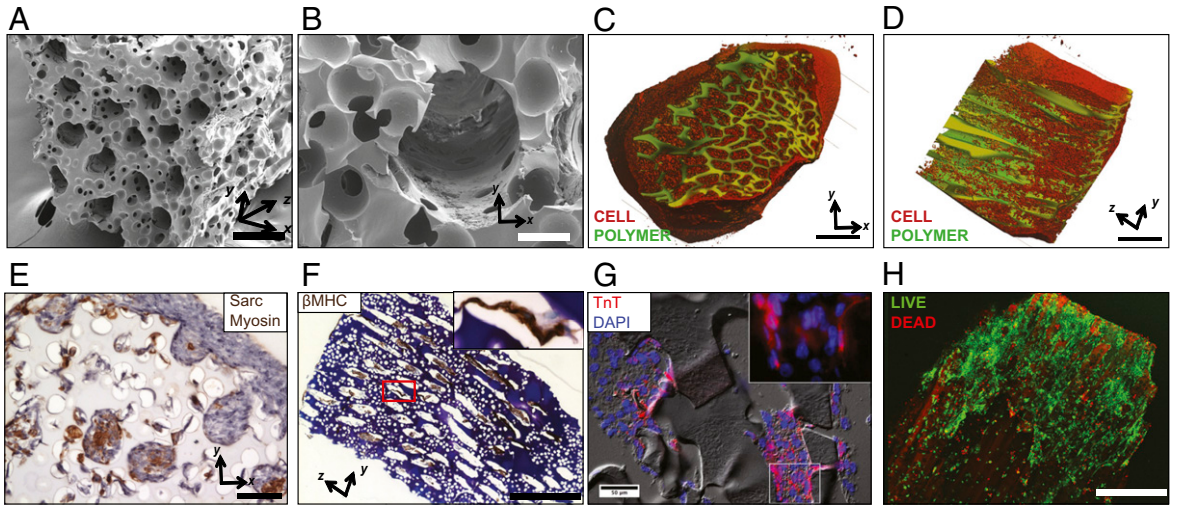

Fig. 1. Analysis of bimodal scaffolds in vitro. (*A* and *B*) SEM images of bimodal scaffolds. Final scaffold design consists of 60-μm channels spaced 60 μm apart. Channel walls contain spherical pores with a 30-μm diameter and 15-μm interconnects. Note that the dehydrated structures are ~80% of their hydrated size. (*C* and *D*) Digital volumetric imaging shows a fiber-templated scaffold (green) seeded with primary chick cardiomyocytes (red). Seeding is uniform across the channels (*C*), whereas the longitudinal cross-section (*D*) reveals a slight gradient in cell density. (*E*) Chick cardiomyocyte-seeded structure with positive staining for sarcomeric myosin heavy chain (Sarc; brown). Cardiomyocytes reside predominantly within the channels, whereas noncardiomyocytes migrate throughout the pores. (*F*) hESC-CM–seeded scaffolds cultured for 1 wk showing a high density of β-myosin heavy chain–positive (brown) cells within the channels. This scaffold measures ~600 μm perpendicular to the page with this section taken at the midpoint, ~300 μm into the scaffold. (*Inset*) The 40× magnification image shows that cardiomyocytes at the center of the construct exhibit shrunken cytoplasm, but intact nuclei indicate viability. (*G*) Immunolabeling against troponin T shows the presence of contractile proteins in hESC-CM seeded in the channel constructs. (*Inset*) The 100× magnification of the boxed area shows troponin T–positive hESC-CM oriented along scaffold channels. (*H*) Confocal image obtained using a live/dead assay shows the distribution of cells relative to the channel constructs (autofluorescent in red). (Scale bars: *A*, 100 μm; *B*, 20 μm; *C* and *D*, 300 μm; *E*, 50 μm; *F*, 400 μm; *G*, 50 μm; H, 400 μm.)

Our human embryonic stem cell (hESC) differentiation protocol yielded cell preparations of 10–65% cardiac purity that were enhanced by Percoll gradient centrifugation. In contrast to the noncardiomyocyte-dominated constructs of chick-derived cardiomyocytes, scaffolds seeded with hES-derived cardiomyocytes (hESC-CM) became enriched with cardiomyocytes. In every experiment, nonmyocytes declined over 5-d culture in serum-free medium, resulting in predominantly cardiomyocytes (~95% β-myosin heavy chain–positive) organized within scaffold channels. Thus, porous channel walls were free of cells and available for mass transfer (Fig. 1*F*). Enhanced mass transfer by segregation of cardiomyocytes and reduction of the noncardiomyocyte population allowed culture of larger constructs with minimal core death. Cells remained viable up to 300 μm from the scaffold edge under static culture as shown by live/dead staining (Fig. 1*H*). Cardiomyocytes expressed the contractile proteins β-myosin heavy chain (Fig. 1*F*) and troponin T (Fig. 1*G*). These embryonic-stage cardiomyocytes did not fully assemble sarcomeres but still contracted with sufficient force to deform the polymer scaffold (Movie S1).

Density of seeded β-myosin heavy chain–positive cardiomyocytes was determined from sections of several constructs. Although limited to the channels (25% construct volume), hESC-CM density ($42 \pm 10 \times 10^6/\text{cm}^3$) compared favorably with cardiomyocyte density in adult human heart ($20 \times 10^6/\text{cm}^3$) (15). The small size of hESC-CM relative to already hypertrophied adult cardiomyocytes permitted such high loadings. Construct cardiomyocyte density may increase over time, because hESC-CM maintain their proliferative capacity for at least 2 wk in culture (Fig. S1).

Myocardial Response to Acellular Constructs. In vivo studies were performed to evaluate the impact of pore size on fibrous encapsulation and vascularization of collagen-modified pHEMA-co-MAA hydrogels in cardiac tissue. Previously, our group showed that fibrous encapsulation and vascularization are sensitive to pore size for s.c. implants in mice (10). The current studies examined such effects for myocardial implants in both athymic nude and immunocompetent rats. A 4-wk time point was used for histological analysis to understand long-term consequences of implants, because the acute and chronic inflammatory responses to biomedical implants subside by 3 wk (16, 17).

Representative images of the myocardial response to 30-μm pore constructs in the nude rat are shown in Fig. 2 *A–D*. H&E stain shows the construct bordered by a thin, fibrous capsule, whereas the pores and surrounding interface are filled with granulation tissue (Fig. 2 *A* and *B*). Neovascularization was observed by immunostaining for the rat endothelial cell marker RECA-1 (Fig. 2*C*). Lumen structures were found within the construct and in adjacent fibrous tissue. Implant vascularization in the nude rat was quantified by the number of RECA-1^+ lumens per unit area. Fig. 2*I* shows that a pore size threshold exists for lumen formation that probably is a function of the throat size connecting adjacent pores, ~40–50% of the pore size. Lumen density was statistically equivalent for 30- and 60-μm pore constructs. Macrophages (MΦ) also were present, confirmed by anti-CD68 immunostaining (Fig. 2*D*). Although MΦ dominated the construct surface, the spherical pores appeared to inhibit foreign body giant cell formation.

Fibrous encapsulation was examined using Masson's trichrome to detect collagen deposition (Fig. 2 *E–H*). This stain confirmed the formation of granulation/fibrous tissue within the porous network. Collagen capsule thickness correlated with pore size, so that 20 μm ≈ 30 μm < 60 μm ≈ solid in the nude rat (Fig. 2*J*). This effect was confirmed in the Sprague-Dawley rat (Fig. S2).

The above observations prompted inquiry into the functionality and mechanism of neovascularization within the scaffolds. In this case, acellular scaffolds of a wider pore size range, up to 80 μm, were implanted into the myocardium of immunocompetent Sprague-Dawley rats for 4 wk. To test functionality of neovasculature, we perfused the rats before they were killed with a biotinylated lectin that binds vessel walls and later was detected by immunostaining (Fig. 3*A*). Density of perfused vessels, quantified over entire

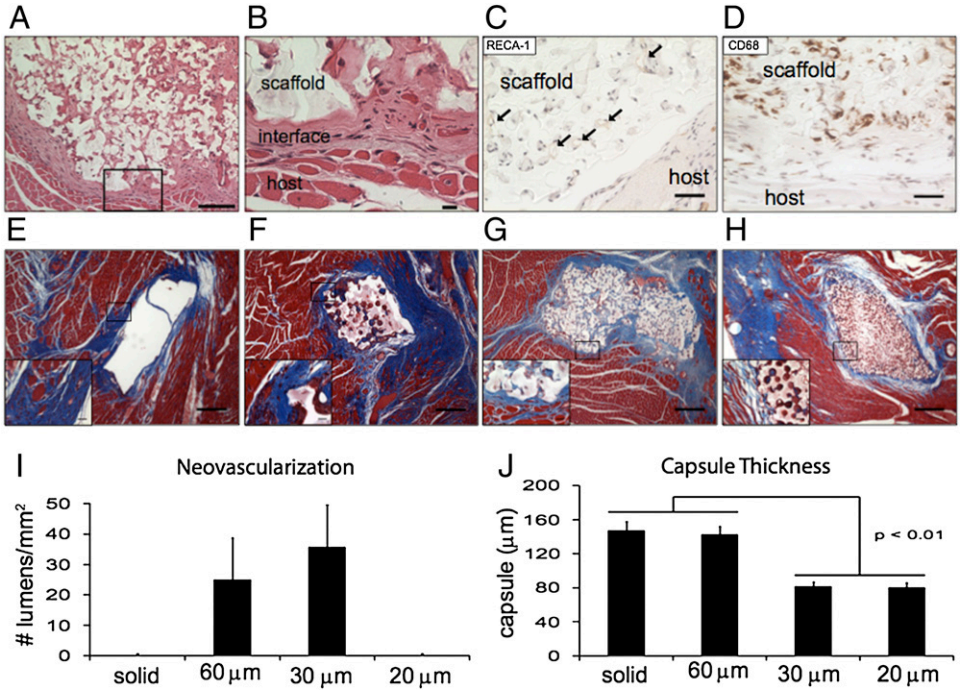

Fig. 2. Acellular scaffolds implanted in the nude rat myocardium for 4 wk. (*A*) H&E overview of the implant, scar, and surrounding myocardium. (*B*) The 20× magnification of the boxed area in *A* shows the thin scar separating the implant from host tissue. Pores are filled primarily with granulation tissue including small vessels. (*C*) Endothelial lumens positive for the rat endothelial cell marker RECA-1 are present in the scaffold (arrows). (*D*) $CD68^+$ macrophages infiltrated porous constructs (brown staining), but porosity limited fusion to foreign body giant cells. (*E–H*) Trichrome staining shows the collagen capsule (blue) and surrounding myocardium (red). (*E*) Nonporous and (*F*) 60-μm porous constructs had thicker and denser capsules than (*G*) 30-μm and (*H*) 20-μm pores. *Insets* show 20× images of boxed areas in *E–H*. (Scale bars: *A*, 100 μm; *B*, 10 μm; *C* and *D*, 50 μm; *E–H*, 250 μm; *Insets*, 50 μm.) (*I*) Neovascularization was assessed by quantification of RECA-1^+ lumen structures ($n = 3$). (*J*) Thickness of the fibrous capsule surrounding implants was measured ($n = 3$).

implant sites, was significantly higher in the implants with pore sizes of 40 and 80 μm (Fig. 3*D*). Observation of a pore-size threshold for perfusion is consistent with the threshold for lumen formation in the nude rat model. Fidelity of the biotinylated lectin as a marker of perfusion was confirmed by colocalization of the biotinylated lectin and endothelial cells (Fig. 3*B*). Additionally, vessels with a smooth muscle layer were identified within the scaffold by double staining for endothelial (RECA-1) and smooth muscle cells (α-smooth muscle actin) (Fig. 3*C*). Because most endothelial structures were perfused with the lectin, and maturation of vessels was evident, these findings suggest functional neovascularization. Thus, we demonstrate that constructs with a 30- to 40-μm pore size achieve maximal vascularization and minimal fibrous encapsulation.

Mechanistically, we examined whether increased neovascularization coincided with a shift in MΦ polarity. Based on the large number of MΦ at the implant site and their known role in directing the foreign body reaction (FBR) (17), we hypothesized that scaffold architecture could impact MΦ activation to the proinflammatory M1 state or the prohealing M2 state (18). MΦs expressing M1 and M2 markers in the scaffold were quantified by triple-label immunofluorescence. CD68 was used as a pan-MΦ marker. Nitric oxide synthase 2 (NOS2) and MΦ mannose receptor (MMR) were representative markers for the M1 and M2 activation states, respectively (18–20) (Fig. 4 *A–D*). Activated $CD68^+$ cells were categorized into three groups: $NOS2^+/MMR^-$, $NOS2^-/MMR^+$, and $NOS2^+/MMR^+$ (Fig. 4*E*).

MΦ phenotype varied with scaffold architecture. A majority of MΦ at implant sites were $NOS2^+/MMR^+$ or $NOS2^+/MMR^-$; $NOS2^-/MMR^+$ cells comprised <20% of all $CD68^+$ cells and tended to be most common in the highly vascular 40-μm scaffolds ($P = 0.06$ versus nonporous). For nonporous scaffolds, ~50% of MΦ were $NOS2^+/MMR^+$. Presence of pores led to an increase in MMR^+ cells. Greater percentages of $NOS2^+/MMR^+$ MΦ were found for all porous implants ($P < 0.05$ versus nonporous). This increased MMR expression, a marker of M2 polarization, suggests a shift toward a prohealing phenotype and may explain the enhanced neovascularization seen for porous scaffolds.

Discussion

We set out to produce a scaffold to promote bundled orientation of cardiomyocytes, increased mass transfer, enhanced neovascularization, and integration with myocardial tissue. We fabricated a biologically analogous scaffold with channel domains for cardiomyocytes and spherical pore domains for mass transfer and invading vasculature, MΦ, and stroma. Sizing of this bimodal, rod-shaped scaffold was based on reported models of mass transfer for cardiac constructs (21) and our empirical observations. A minimum channel diameter of 60 μm was required to seed cardiomyocytes reliably in a 2-mm-long channel by iterative centrifugation. Cell confinement within the 60-μm channel promoted cardiomyocyte aggregation.

Initial experiments using chicken embryonic cardiomyocytes showed that these bimodal scaffolds could be seeded with a high cell density. For this mixed cell population of 20–25% cardiomyocytes, the less-migratory cardiomyocytes principally remained in channels, whereas noncardiomyocytes migrated throughout the porous network. Cardiomyocytes have a high affinity for each other, with increased survival and formation of interconnected networks when cultured at high densities. Although pore space was allocated for mass transfer, nonmyocyte overgrowth limited culture of chick cardiomyocyte constructs to 1 wk.

Unexpectedly, most nonmyocytes in hESC-derived preparations died off after culturing in serum-free media, leaving a construct composed of ~95% cardiomyocytes, regardless of initial heterogeneity. This die-off resulted in interstices free of cells for improved mass transfer and cell survival up to 300 μm into the

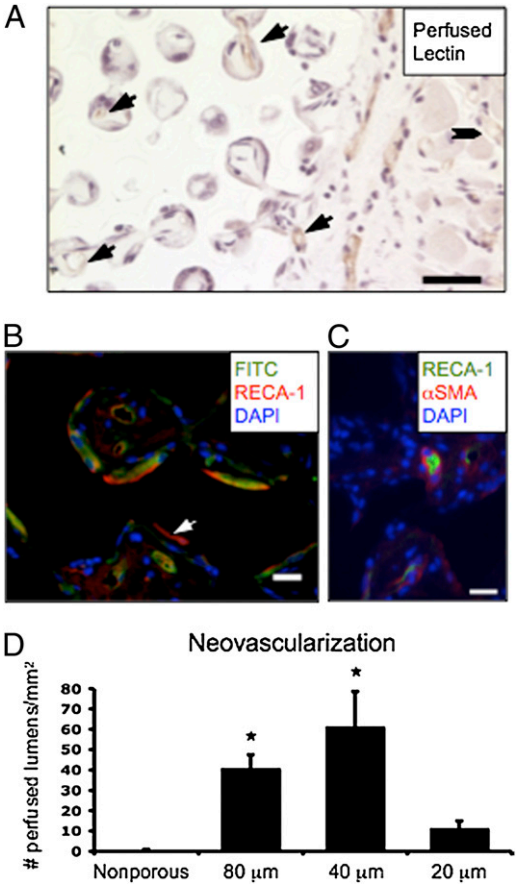

Fig. 3. Evaluation of vessel functionality in 4-wk myocardial implants in Sprague-Dawley rats by biotinylated lectin perfusion. (*A*) Lumen structures positive for biotinylated lectin (brown staining) were identified within porous implants (arrows) and host tissue (dart). (*B*) Perfused biotinylated lectin (streptavidin-FITC) and endothelial cells (RECA-1) were colocalized within the scaffold. Few unperfused endothelial structures were RECA-1$^+$/lectin$^-$ (arrow). (*C*) Mature vessels had RECA-1$^+$ lumens with a smooth muscle layer positive for α-smooth muscle actin. (*D*) Density of functional vessels was quantified over the entire implant with 40- and 80-μm porous scaffolds having significantly higher densities than nonporous and 20-μm porous scaffolds ($n = 4$; $^*P < 0.05$). (Scale bars: *A,* 50 μm; *B* and *C,* 20 μm.)

scaffold. Cells survived >2 wk at this depth under static culture conditions and without oxygen carriers. Importantly, this scaffold design resulted in discrete channels containing physiologically relevant densities of hESC-CM. Furthermore, hESC-CM expressed the contractile proteins β-myosin heavy chain and troponin T. As expected for early embryonic cardiomyocyte development, we did not see widespread sarcomeric organization. Despite the absence of mature sarcomeres, networks of cardiomyocytes, estimated at 20% of the construct volume, generated sufficient contractile force to deform the constructs in vitro. We expect a more organized contractile apparatus to form as hESC-CM mature toward an adult phenotype. Future studies will evaluate the role of mechanical stimulation in maturation and sarcomeric organization by application in vitro or after natural stimulation upon implantation in the heart.

Our approach builds on a few central concepts in cardiac tissue engineering. Spatial control was introduced by McDevitt et al. (22, 23). High densities of cardiomyocytes were obtained by relying on self-aggregation of cardiomyocytes, the basis for scaffold-free systems (3–8). We used a synthetic scaffold designed to organize the cardiomyocytes and facilitate mass transfer (21, 24–28). Our approach differs from previous scaffold-based attempts in that regions were designed to exclude cardiomyocytes. Cell organization into distinct realms, with separation for mass transfer, permitted the formation of larger constructs. Cell densities similar to those in the adult human heart were realized despite the relatively small volume for cardiomyocytes. Moreover, the ability of hESC-CM to proliferate (Fig. S1) (29) may compensate for cell death expected during the transition from in vitro culture to the in vivo environment. Formation of a dense, organized cardiomyocyte network within the channels was encouraging, although additional aspects of the construct remain to be optimized. We predict that scaffold degradation (14) with kinetics timed for revascularization will facilitate host–graft contact, cardiomyocyte expansion and hypertrophy, and cardiomyocyte integration for electromechanical coupling and force generation.

Cardiac implantation of acellular constructs verified the feasibility of using bimodal pHEMA-co-MAA scaffolds for in vivo cell delivery and established a size threshold necessary for vessel lumen formation and perfusion. Beyond this threshold, pore size over the range studied here had no statistically significant impact on vascularization. The density of functional vessels within implants with pore sizes of 40 and 80 μm was similar to previous reports of prevascularized cardiac implants (30) without complications of tricell (cardiomyocyte, endothelial cell, fibroblast) sourcing and seeding. Previous studies by our group found that s.c.-implanted, sphere-templated materials with larger pores (~90–160 μm) led to more fibrosis and less vascularity (10). Constrained by the small size of the rat heart, myocardial response to larger pores (>80 μm) was not determined. Pore size effects observed here relate to previous studies in which 10- to 45-μm pores filled with fibrohistiocytic tissue, whereas pores >45 μm filled with organized fibrous tissue (31, 32). These earlier studies used materials with broad pore-size distributions (only average pore size was reported), making conclusions about the effects of pore size difficult. In contrast, the sphere-templated materials used here had tightly controlled pore and interconnect sizes.

MΦ phenotype was explored as a mechanism by which scaffold architectures enhanced neovascularization. MΦ orchestrate the FBR by releasing cytokines and chemical mediators to attract other cells (endothelial cells, MΦ, fibroblasts) and to break down the implant (17). These MΦ are activated over a proposed polarization continuum (M1/M2 polarization) (18–20). At one end, M1-polarized MΦ are proinflammatory; at the other extreme, M2-polarized MΦ are considered antiinflammatory, marked by the release of growth factor and tissue remodeling (19, 33). Here we find that MΦ activation depends on biomaterial architecture in addition to previously implicated biomaterial chemistry and bioactivity (34–36).

Representative markers of the M1 and M2 activation states, NOS2 and MMR, respectively, were used to elucidate the activation state of implant-associated MΦ. A majority of the activated MΦ expressed NOS2, indicating the biomaterial activates proinflammatory pathways. MMR expression increased significantly at porous implants, and this increase tracked with improved neovascularization for implants with pores >20 μm. The increase in MMR expression resulted in a large fraction of MΦ of a mixed phenotype at porous implants, showing that a defined porous architecture turns on supposed pro-healing pathways in these NOS2$^+$ MΦ. Previous in vivo studies demonstrated concurrent expression of M1 and M2 markers (37), and enhanced expression of M2 markers has been associated with improved outcomes for implanted biologic scaffolds (34). Our results are consistent with these studies: MΦ activation to an M2 phenotype coincides with enhanced neovascularization. Future studies will examine additional macrophage-activation markers and cytokine expression to determine where scaffold-associated macrophages lie on the polarization continuum and to what extent they direct neovascularization.

This work describes a proangiogenic, bimodal scaffold for cardiac tissue engineering. The scaffold was tailored to accommodate

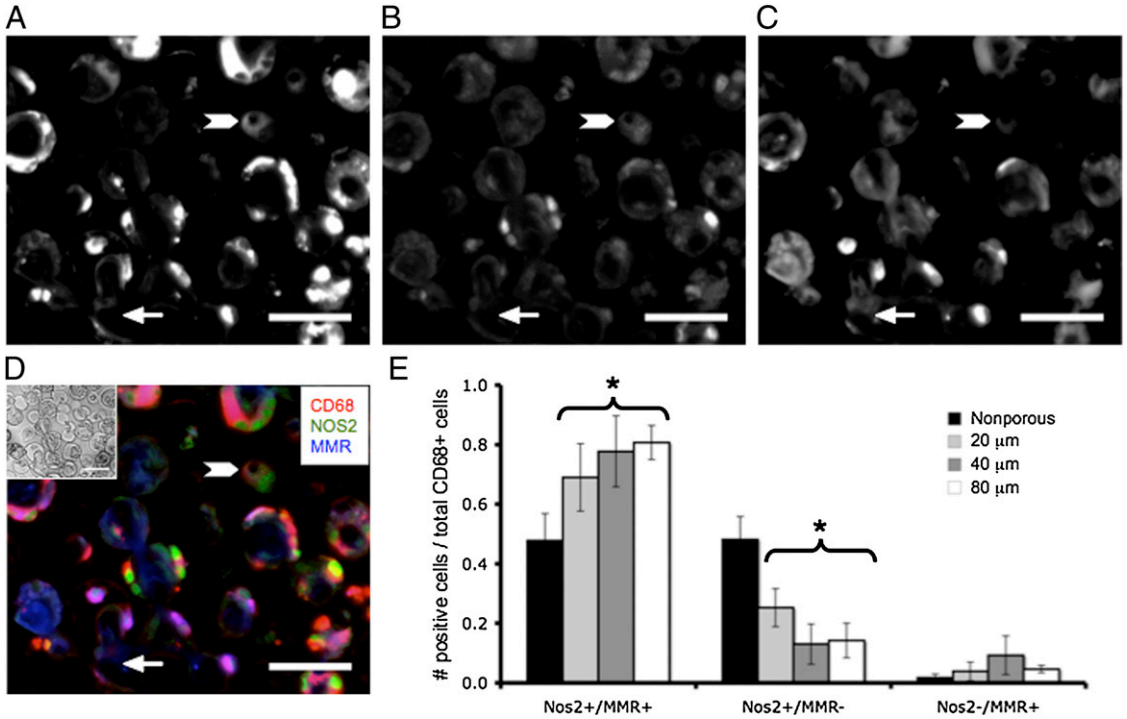

Fig. 4. Macrophage phenotype in response to 4-wk myocardial implants in Sprague-Dawley rats. (*A*) MΦ were identified with CD68$^+$ staining. M1 and M2 phenotypes were determined by NOS2 (*B*) and MMR (*C*), respectively. (*D*) Overlayed images of CD68, NOS2, and MMR were analyzed to determine MΦ phenotype. A majority of MΦ in the porous implants expressed both NOS2 and MMR, although NOS2$^+$/MMR$^-$ (darts) and NOS2$^-$/MMR$^+$ (arrows) MΦ could be identified (*A*–*D*). MΦ typically adhered to the material (*D*, brightfield *Inset*). (*E*) The fraction of each activated state was determined for CD68$^+$ MΦ, with significant increase in NOS2$^+$/MMR$^+$ MΦ at all porous implant sites ($n = 4$; $P < 0.05$). There is a trend of increased NOS2$^-$/MMR$^+$ MΦ in 40-μm porous constructs versus nonporous ($P = 0.06$). (Scale bars: *A*–*D*, 50 μm.)

the propensity of cardiomyocytes to aggregate within aligned channels optimized to attain constructs approximating in vivo cell densities. In acellular cardiac implants, the sphere-templated architecture maximized neovascularization while minimizing fibrosis. We developed a model system for ongoing studies on hESC-CM behavior and cardiac tissue engineering. Rod-like scaffold constructs could feasibly be implanted in infarcted human hearts using minimally invasive catheter introduction systems.

Materials and Methods

Scaffold Fabrication. Bimodal scaffolds having interconnected spherical pore regions and channels with high aspect ratios were templated from poly (methyl methacrylate) (PMMA) beads and polycarbonate (PC) core/PMMA optical fiber (POF) shell according to published methods (10, 13) with slight modifications (*SI Materials and Methods*). The template was infiltrated with monomer solution (2-HEMA and 5% MAA) using tetraethylene glycol dimethacrylate as a cross-linker and Irgacure 651 (Ciba) as a UV initiator (38). The PC/PMMA template was solubilized in dichloromethane over 5 d; then the hydrogel was rehydrated to water and surface derivatized with rat tail collagen I (BD) using ethyl(dimethylaminopropyl) carbodiimide/N-hydroxysuccinimide (EDC/NHS) chemistry.

Cardiomyocyte Isolation. Cardiomyocytes were isolated from day 11 chicken embryos as previously described (39) (*SI Materials and Methods*). HESC-CM were obtained using protocols developed in our laboratories (40) (*SI Materials and Methods*).

Cell Seeding of Constructs. Gels, 2 mm thick, were punched out using a 3-mm biopsy punch, with channels parallel to the punch. With the gel in the biopsy punch, 5 million cells in 50 μL of medium were loaded on top of the gel. The construct was placed in a 1.7-mL Eppendorf tube and centrifuged for 5 min at ~200 × *g*. The construct was washed with medium to remove and collect cells that had not entered channels. This process was repeated three times. Constructs were removed from the biopsy punch and cut into strips ~300–800 μm thick × 2 mm long. At the appropriate time, samples were fixed and histologically analyzed (*SI Materials and Methods*).

Digital Volumetric Imaging. Chick cardiomyocyte-seeded scaffolds were fixed and subject to whole-mount fluorescent staining using acridine orange for cell nuclei (red) and eosin Y for cytoplasm (green). Samples were processed and sectioned in a Digital Volumetric Imager (Microscience Group) (41). Sections were taken and the block imaged at 1-μm intervals with a 10× objective at ~0.9 μm/voxel using 460–500 nm excitation light and emission filters for >600 nm (red) or 510–590 nm (green). Images were reconstructed into a 3D representation using ResView version 3.2 (Microsciences Group). Scaffolds displayed nonspecific acridine orange/eosin staining, resulting in high-intensity red/green fluorescence (yellow upon overlay). Overlap of acridine orange also was seen in the cell cytoplasm, resulting in the red appearance of most cellular material (*SI Materials and Methods*).

Acellular Myocardial Implants. All animal experiments adhered to federal guidelines and were approved by the University of Washington Animal Care and Use Committee. Athymic nude rats (Rh-rnu/rnu) and Sprague-Dawley rats were used to evaluate myocardial implantation of acellular, collagen-modified pHEMA-co-MAA scaffolds of varying pore size (*SI Materials and Methods*). At 28 d, animals were killed with pentobarbital; hearts were removed, rinsed in PBS, and fixed in methyl Carnoy's solution. Sprague-Dawley rats, used in analysis of vessel perfusion and MΦ activation, were anesthetized with isoflurane and injected with 300 μg biotinylated tomato lectin (Vector Labs) 28 d after implantation and 10 min before they were killed. Hearts were vibratomed to 1-mm-thick sections, routinely processed, paraffin embedded, and sectioned for histological analysis. FBR was evaluated by H&E and trichrome stains; immunohistochemistry was performed to detect endothelial cells, macrophages, and smooth muscle cells; vessel functionality was assessed by detection of perfused biotinylated lectin (*SI Materials and Methods*). Images were acquired on a Nikon TE200 inverted or an E800 upright microscope in brightfield or epifluorescence using Metamorph software.

Statistical Analysis. Data are presented as means ± 95% confidence intervals. Quantification of histological sections was performed with 40× images taken

over the entire implant area on two or three sections per animal ($n = 3$ or 4). A paired t test was used to establish significance.

ACKNOWLEDGMENTS. We thank Kelly Stevens, Nate Tulloch, Lil Pabon, Veronica Muskheli, Jennifer Deem, Ben Van Biber, Yiheng Lie, Wei Xing, and Stephanie Bryant for useful discussions. This work was funded by National Institutes of Health Grants R01 HL64387 (to B.D.R. and C.E.M.), P01 HL094374 (to C.E.M.), and R01 HL084642 (to C.E.M.). Animal studies were supported by University of Washington Mouse Metabolic Phenotyping Center Grant U24 DK076126 (to C.E.M.).

1. Müller-Ehmsen J, et al. (2002) Survival and development of neonatal rat cardiomyocytes transplanted into adult myocardium. *J Mol Cell Cardiol* 34:107–116.
2. Zhang M, et al. (2001) Cardiomyocyte grafting for cardiac repair: Graft cell death and anti-death strategies. *J Mol Cell Cardiol* 33:907–921.
3. Shimizu T, et al. (2002) Fabrication of pulsatile cardiac tissue grafts using a novel 3-dimensional cell sheet manipulation technique and temperature-responsive cell culture surfaces. *Circ Res* 90:e40.
4. Stevens KR, Pabon L, Muskheli V, Murry CE (2009) Scaffold-free human cardiac tissue patch created from embryonic stem cells. *Tissue Eng Part A* 15:1211–1222.
5. Kelm JM, et al. (2006) Tissue-transplant fusion and vascularization of myocardial microtissues and macrotissues implanted into chicken embryos and rats. *Tissue Eng* 12:2541–2553.
6. Zimmermann WH, et al. (2002) Cardiac grafting of engineered heart tissue in syngenic rats. *Circulation* 106(12)(Suppl 1):I151–I157.
7. Zimmermann WH, Melnychenko I, Eschenhagen T (2004) Engineered heart tissue for regeneration of diseased hearts. *Biomaterials* 25:1639–1647.
8. Zimmermann WH, et al. (2006) Engineered heart tissue grafts improve systolic and diastolic function in infarcted rat hearts. *Nat Med* 12:452–458.
9. Robey TE, Saiget MK, Reinecke H, Murry CE (2008) Systems approaches to preventing transplanted cell death in cardiac repair. *J Mol Cell Cardiol* 45:567–581.
10. Marshall AJ, et al. (2004) Biomaterials with tightly controlled pore size that promote vascular in-growth. *Polymer Preprints* 45:100–101.
11. Isenhath SN, et al. (2007) A mouse model to evaluate the interface between skin and a percutaneous device. *J Biomed Mater Res A* 83:915–922.
12. Kléber AG, Rudy Y (2004) Basic mechanisms of cardiac impulse propagation and associated arrhythmias. *Physiol Rev* 84:431–488.
13. Stokols S, Tuszynski MH (2004) The fabrication and characterization of linearly oriented nerve guidance scaffolds for spinal cord injury. *Biomaterials* 25:5839–5846.
14. Atzet S, Curtin S, Trinh P, Bryant S, Ratner B (2008) Degradable poly(2-hydroxyethyl methacrylate)-co-polycaprolactone hydrogels for tissue engineering scaffolds. *Biomacromolecules* 9:3370–3377.
15. Olivetti G, Capasso JM, Sonnenblick EH, Anversa P (1990) Side-to-side slippage of myocytes participates in ventricular wall remodeling acutely after myocardial infarction in rats. *Circ Res* 67:23–34.
16. Anderson JM (1988) Inflammatory response to implants. *ASAIO Trans* 34:101–107.
17. Anderson JM, Rodriguez A, Chang DT (2008) Foreign body reaction to biomaterials. *Semin Immunol* 20:86–100.
18. Arnold SA, et al. (2010) Lack of host SPARC enhances vascular function and tumor spread in an orthotopic murine model of pancreatic carcinoma. *Dis Model Mech* 3: 57–72.
19. Martinez FO, Helming L, Gordon S (2009) Alternative activation of macrophages: An immunologic functional perspective. *Annu Rev Immunol* 27:451–483.
20. Mantovani A, et al. (2004) The chemokine system in diverse forms of macrophage activation and polarization. *Trends Immunol* 25:677–686.
21. Radisic M, Deen W, Langer R, Vunjak-Novakovic G (2005) Mathematical model of oxygen distribution in engineered cardiac tissue with parallel channel array perfused with culture medium containing oxygen carriers. *Am J Physiol Heart Circ Physiol* 288: H1278–H1289.
22. McDevitt TC, et al. (2002) In vitro generation of differentiated cardiac myofibers on micropatterned laminin surfaces. *J Biomed Mater Res* 60:472–479.
23. McDevitt TC, Woodhouse KA, Hauschka SD, Murry CE, Stayton PS (2003) Spatially organized layers of cardiomyocytes on biodegradable polyurethane films for myocardial repair. *J Biomed Mater Res A* 66:586–595.
24. Freed LE, Vunjak-Novakovic G (1997) Microgravity tissue engineering. *In Vitro Cell Dev Biol Anim* 33:381–385.
25. Carrier RL, et al. (2002) Effects of oxygen on engineered cardiac muscle. *Biotechnol Bioeng* 78:617–625.
26. Bursac N, et al. (1999) Cardiac muscle tissue engineering: Toward an in vitro model for electrophysiological studies. *Am J Physiol* 277:H433–H444.
27. Radisic M, et al. (2006) Oxygen gradients correlate with cell density and cell viability in engineered cardiac tissue. *Biotechnol Bioeng* 93:332–343.
28. Papadaki M, et al. (2001) Tissue engineering of functional cardiac muscle: Molecular, structural, and electrophysiological studies. *Am J Physiol Heart Circ Physiol* 280: H168–H178.
29. McDevitt TC, Laflamme MA, Murry CE (2005) Proliferation of cardiomyocytes derived from human embryonic stem cells is mediated via the IGF/PI 3-kinase/Akt signaling pathway. *J Mol Cell Cardiol* 39:865–873.
30. Lesman A, et al. (2010) Transplantation of a tissue-engineered human vascularized cardiac muscle. *Tissue Eng Part A* 16:115–125.
31. White R, et al. (1983) Effect of healing on small internal diameter arterial graft compliance. *Biomater Med Devices Artif Organs* 11:21–29.
32. Beahan P, Hull D (1982) A study of the interface between a fibrous polyurethane arterial prosthesis and natural tissue. *J Biomed Mater Res* 16:827–838.
33. Sica A, et al. (2008) Macrophage polarization in tumour progression. *Semin Cancer Biol* 18:349–355.
34. Brown BN, Valentin JE, Stewart-Akers AM, McCabe GP, Badylak SF (2009) Macrophage phenotype and remodeling outcomes in response to biologic scaffolds with and without a cellular component. *Biomaterials* 30:1482–1491.
35. Badylak SF, Valentin JE, Ravindra AK, McCabe GP, Stewart-Akers AM (2008) Macrophage phenotype as a determinant of biologic scaffold remodeling. *Tissue Eng Part A* 14: 1835–1842.
36. Brodbeck WG, et al. (2003) *In vivo* leukocyte cytokine mRNA responses to biomaterials are dependent on surface chemistry. *J Biomed Mater Res A* 64:320–329.
37. Daley JM, Brancato SK, Thomay AA, Reichner JS, Albina JE (2010) The phenotype of murine wound macrophages. *J Leukoc Biol* 87:59–67.
38. Ratner BD, Miller IF (1973) Transport through crosslinked poly(2-hydroxyethyl methacrylate) hydrogel membranes. *J Biomed Mater Res* 7:353–367.
39. Iwaki K, Sukhatme VP, Shubeita HE, Chien KR (1990) Alpha- and beta-adrenergic stimulation induces distinct patterns of immediate early gene expression in neonatal rat myocardial cells. fos/jun expression is associated with sarcomere assembly; Egr-1 induction is primarily an alpha 1-mediated response. *J Biol Chem* 265:13809–13817.
40. Laflamme MA, et al. (2007) Cardiomyocytes derived from human embryonic stem cells in pro-survival factors enhance function of infarcted rat hearts. *Nat Biotechnol* 25: 1015–1024.
41. Ewald AJ, McBride H, Reddington M, Fraser SE, Kerschmann R (2002) Surface imaging microscopy, an automated method for visualizing whole embryo samples in three dimensions at high resolution. *Dev Dyn* 225:369–375.